ANL/TD/CP-94009
CONF-9705211--

Dynamic Behavior of Plasma-Facing Materials during Plasma Instabilities in Tokamak Reactors

A. Hassanein

Argonne National Laboratory, USA

I. Konkashbaev

Troitsk Institute for Innovation and Fusion Research, Russia

Invited paper presented at the Sixth All-Russian Conference on Engineering Problems of Thermonuclear Reactors, EPTR-6, St. Petersburg, Russia, May 25-29, 1997.

Also accepted for publications in **Plasma Devices and Operations**, July 1997.

DISCLAIMER

Dynamic Behavior of Plasma-Facing Materials during Plasma Instabilities in Tokamak Reactors

A. Hassanein[1] and I. Konkashbaev[2]

[1]Argonne National Laboratory, Argonne, IL 60439, USA

[2]Troitsk Institute for Innovation and Fusion Research, Troitsk, Russia

Abstract

Damage to plasma-facing and nearby components due to plasma instabilities remains a major obstacle to a successful tokamak concept. The high energy deposited on facing materials during plasma instabilities can cause severe erosion, plasma contamination, and structural failure of these components. Erosion damage can take various forms such as surface vaporization, spallation, and liquid ejection of metallic materials. Comprehensive thermodynamic and radiation hydrodynamic codes have been developed, integrated, and used to evaluate the extent of various damage to plasma-facing and nearby components. The eroded and splashed materials will be transported and then redeposited elsewhere on other plasma-facing components. Detailed physics of plasma/solid-liquid/vapor interaction in a strong magnetic field have been developed, optimized, and implemented in a self-consistent model. The plasma energy deposited in the evolving divertor debris is quickly and intensely reradiated, which may cause severe erosion and melting of other nearby components. Factors that influence and reduce vapor-shielding efficiency such as vapor diffusion and turbulence are also discussed and evaluated.

1. Introduction

Damage to plasma-facing components (PFCs) and structural materials due to loss of plasma confinement in magnetic fusion reactors remains one of the most serious concerns for safe, successful, and reliable reactor operation. Plasma instabilities can take various forms such as hard disruptions, which include both thermal and current quench, edge-localized modes (ELMs), and vertical displacement events (VDEs). The intense energy deposition (10-200 MJ/m^2) in these events over a short period (0.1-300 ms) may result in severe surface and bulk damage [1]. Surface damage includes high erosion losses due to surface vaporization, spallation, and melt-layer loss. Bulk damage effects include large temperature increases in structural materials and at the interface between surface coatings and structural materials. These large temperature increases will cause high thermal stresses, possible melting, and material fatigue and failure. Other bulk effects of some plasma instabilities, particularly those of longer duration such as VDEs and those with deeper deposited energy such as runaway electrons, can cause high heat flux levels at the coolant channels; this may cause burnout of these tubes and result in significant down-times for repair and maintenance [2]. In addition to these effects, the transport and redeposition of the eroded surface materials from vaporization, melt-layer splashing, and macroscopic particle emission to various locations on plasma-facing and nearby components are of major concern for safety, plasma contamination, and successful and prolonged

plasma operations following plasma instability events [3]. A procedure to clean up the redeposited debris of the eroded materials should be as important as the procedure to repair the incurred damage on PFCs.

The initial stage of energy deposited during plasma instabilities is known to cause sudden formation of a vapor cloud above the exposed area. This vapor cloud, if well confined, may significantly reduce the net energy flux to the original disruption location, thus substantially reducing vaporization losses. Detailed physics of plasma/solid-liquid/vapor interactions in a strong and oblique magnetic field have been developed and evaluated in a comprehensive self-consistent manner. Such detailed treatment of the magnetohydrodynamics and photon radiation transport in the vapor-cloud region, for example, are very important in determining the net erosion thickness from surface vaporization [4].

The extent of the resulting damage to plasma-facing materials (PFMs), structural materials, and coolant channels depends mainly on the total plasma energy deposited, deposition time, and thickness and type of armor material. During the short disruption events ($\tau_d \leq 1$ ms), the initially evaporated material may significantly reduce further PFM vaporization erosion. The stability and confinement of this vapor plasma during the disruption is therefore a very important issue in evaluating the overall lifetime of PFCs. Models to study and evaluate hydrodynamic instabilities that cause the loss of vapor plasma during

the disruption have been developed. During longer plasma instabilities, however, such as VDEs ($\tau_d \geq 100$ ms) or runaway electrons, no significant self-shielding is expected to occur and therefore serious erosion, melting, and structural damage can occur [2]. In addition, hydrodynamic instabilities and other forces will further erode melt layers of metallic PFMs [5]. The amount of melt-layer loss will depend on many parameters, such as duration of melt layer in the liquid phase, melt-layer thickness, and magnitude and direction of various existing forces. Longer plasma instabilities will also allow enough time for the deposited plasma energy to be conducted from the surface to the structural material and finally to the coolant channels where it can cause burnout [2].

Because the heat loads and disruption conditions of the near-term and future tokamak reactors are not achievable in current tokamak machines, laboratory experiments are used to study and simulate disruption effects. Modeling of these experiments and their relevancy to reactor conditions during a disruption are discussed. Because erosion losses of the more relevant simulation experiments to ITER conditions are very small, data on plasma/vapor interaction during simulated disruptions are analyzed and discussed.

2. Brief description of the integrated models

The comprehensive models developed in the A*THERMAL-S and SPLASH codes have been extensively used and are continuously being enhanced to evaluate PFCs response to plasma instabilities [5-7]. In these models, four major modeling stages of plasma/material interaction were developed and integrated with sufficient detail to accurately simulate the effect of plasma instabilities on PFMs. Initially, the incident plasma particles from the disrupted plasma will deposit their energy on PFM surfaces. Models for particle deposition and material thermal evolution that take into account phase change, moving boundaries, and temperature-dependent thermophysical properties, etc., were developed to predict the behavior of these components. This initial pulse of energy delivered to the surfaces of PFMs from the direct impact of plasma particles will cause sudden ablation of these materials. As a result, a vapor cloud from the PFM debris will form in front of the incoming plasma particles. Shortly thereafter, the plasma particles will be completely stopped in this vapor cloud. Continuous heating of the vapor cloud will ionize, excite, and generate photon radiation. The initial plasma particle kinetic energy is therefore quickly transformed into radiation energy.

Comprehensive models for the hydrodynamics and heating of the vapor cloud that shields the original surface were developed for the second stage of disruption modeling. As a result, models for photon radiation emission and transport throughout the vapor cloud regions were developed to estimate the net heat flux transmitted to the facing materials. Because of the importance of

radiation transport in the vapor cloud region, a self-consistent multidimensional approach to calculate realistic and time-dependent radiation field is also developed and implemented in the A*THERMAL-S code [8]. The optical properties of the vapor-cloud-generated plasma are calculated at each time step during the course of disruption. The atomic data base of candidate materials are calculated with the SUPERATOM code [9] and then implemented in the A*THERMAL-S code. This includes all possible transition energy levels, ionization potentials, rate coefficients, photoionization, statistical distribution, oscillator strengths, etc. The rate equations are then solved for each level population at the each corresponding time step. The radiation transport equation is then solved separately for both line-and continuum-generated spectra. The self-consistent model also takes into account the multispecies effect, i.e., mixing between the incoming plasma particles and the vaporized material. This has turned out to be important in explaining fine atomic physics details in disruption simulation experiments.

Detail effects of a strong magnetic field on vapor magnetohydrodynamics (MHD) and subsequent effects were developed and studied. The model includes effects such as 2-D vapor expansion along and parallel to field lines, magnetic field diffusion in the vapor cloud, magnetic and friction forces and Joule heating of the vapor [7]. The reactor magnetic field may limit vapor expansion normal to the divertor surface. This can be particularly important in the case of a closed divertor configuration because the expanding hot vapor

plasma can significantly damage other nearby components not directly exposed to plasma instabilities [10]. In addition, because the developed vapor cloud is critically important in protecting the original disruption location, models to investigate the stability of this vapor-cloud plasma and its confinement by the in-reactor magnetic field have been developed and are discussed here.

Models to study melt-layer behavior of metallic PFCs during plasma instabilities were also developed and implemented in the SPLASH code [11-12]. The melt-layer thickness of the metallic PFCs can be one to two orders of magnitude higher than surface vaporization losses [6]. The free surface of the melt layer during a plasma instability is exposed to various forces such as electromagnetism, gravitation, mechanical vibration, plasma momentum, surface tension, and ablation recoil. Several mechanisms can cause melt-layer loss and ejection during the thermal quench phase of the disruption [7]. These include melt splashing from boiling of gas bubbles, splashing due to absorption of plasma momentum, erosion from hydrodynamic instabilities developed in the liquid layer due to the tangential and perpendicular forces acting on the free surface of the liquid, erosion due to runoff of melt layers over the structure, and erosion caused by mechanical vibration of the machine during the disruption event. Detail models and results of melt-layer splashing and erosion are given in Reference [12].

The correct evaluation of the resulting damage and erosion of PFCs therefore requires an integrated and simultaneous solution of a four-moving-boundaries problem. One moving boundary determined from the solution of vapor hydrodynamic equations is the front of the vapor cloud generated from the initial plasma energy deposition. The second moving boundary due to surface vaporization of the target is calculated from target thermodynamics. Immediately following the surface vaporization front is a third moving boundary due to the melt layer splashing front. Finally, the fourth moving boundary is the liquid/solid interface, which further determines the new thickness of the melt layer. These moving boundaries are interdependent, and a self-consistent solution must link them dynamically and simultaneously. It is the liquid splashing front, however, that determines the extent of metallic PFC erosion and lifetime due to various plasma instabilities.

It is therefore the dynamics and evolution of this vapor cloud that will finally determine the net surface erosion rate and the extent of damage to structural materials and coolant tubes during plasma instabilities. A schematic illustration of the different interaction zones of plasma particles with the divertor vapor/solid-liquid/ surface coating, interface and structural materials, and coolant channels in a strong magnetic field environment is shown in Fig. 1. Coordinate x is the toroidal direction, z is the poloidal direction, and y is the normal direction above the target surface.

3. Dynamic evolution of vapor cloud

Vapor expansion into the vacuum above the exposed target surface under the influence of a strong magnetic field is determined by solving the vapor MHD equations for conservation of mass, momentum, and energy:

$$\frac{\partial \rho}{\partial t} + \nabla \cdot (\rho \mathbf{V}) = 0 \ , \tag{1}$$

$$\rho \frac{\partial \mathbf{V}}{\partial t} + \nabla P = \mathbf{F} \ , \tag{2}$$

and

$$\frac{\partial E}{\partial t} + \nabla \cdot (E\mathbf{V}) + P \, \nabla \cdot \mathbf{V} = \nabla \cdot (K \nabla T) + \nabla \cdot Q_r + \nabla \cdot Q_b \ , \tag{3}$$

where V is vapor velocity, ρ is density, E is energy, P is pressure, **F** is external force, K is vapor conductivity, T is temperature, Q_r is radiation flux, and Q_b is the incident particle flux from the disrupting plasma. All variables of these equations are both time- and space-dependent. The vapor plasma, once fully ionized, is assumed to move freely along magnetic field lines, as shown in Fig. 1. One needs to solve the vapor equation of motion in two directions: along and perpendicular to divertor surface. The radiation transport equations are not

directly affected by the magnetic field and can be solved in one or two dimensions.

The vapor equation of motion in a strong magnetic field environment can be written as

$$\rho \frac{d\mathbf{V}}{dt} = -\nabla P + \mathbf{F}_m, \tag{4}$$

$$\mathbf{F}_m = \frac{1}{c}[\mathbf{J} \times \mathbf{B}], \tag{5}$$

where $\mathbf{F}_m$ is magnetic force, **J** is vapor plasma current density, c is speed of light, and **B** is magnetic flux density. The induced magnetic force will act as a retarding force to vapor expansion. The electric, $\mathcal{E}$, and magnetic fields are defined from Maxwell equations:

$$\frac{1}{c}\frac{\partial \mathcal{E}}{\partial t} = \nabla \times \mathbf{B} + \frac{4\pi}{c}\mathbf{J} \tag{6}$$

$$\frac{1}{c}\frac{\partial \mathbf{B}}{\partial t} = -\nabla \times \mathcal{E}. \tag{7}$$

The time variation of the induced electric field in the vapor plasma is usually very small. Therefore,

$$\nabla \mathrm{x} \mathbf{B} = -\frac{4\pi}{c}\mathbf{J}\text{, and} \tag{8}$$

$$\varepsilon = \frac{1}{c}[\mathbf{V} \mathrm{x} \mathbf{B}] + \frac{\mathbf{J}}{\sigma}, \tag{(9)}$$

where σ is vapor conductivity. The time-varying magnetic field in the vapor plasma can then be given by

$$\frac{\partial \mathbf{B}}{\partial t} = -\nabla \mathrm{x} [\mathbf{V} \mathrm{x} \mathbf{B}] + \nabla \mathrm{x} \left[\frac{c^2}{4\pi\sigma}\nabla \mathrm{x} \mathbf{B}\right]. \tag{10}$$

The magnetic force, $\mathbf{F_m}$, is composed of a magnetic pressure force, $\mathbf{F_p}$, and a tension force, $\mathbf{F_t}$, due to the curvature of the magnetic field lines, where

$$\mathbf{F_p} = \frac{1}{4\pi}(\mathbf{B}\nabla)\mathbf{B} \tag{11}$$

$$\mathbf{F_t} = -\nabla\left(\frac{B^2}{8\pi}\right) \tag{12}$$

For a weakly ionized vapor plasma, conductivity is given by

$$\sigma = \frac{4\pi n_e e^2}{m_e}\tau, \qquad (13)$$

where n_e is density, e is charge, m_e is mass of the electron, and τ is vapor plasma collision time.

The collision time is given by

$$\frac{1}{\tau} = \sum_j \frac{1}{\tau_j}, \qquad (14)$$

where τ_j is the electron collision time with species j where j is index for electron, ion, and neutral particles. The above equations are solved in 2-D coordinates, i.e., along and across the magnetic field lines. The solution is then transformed to the x (along divertor surface) -y (normal to divertor surface) coordinates as shown in Fig. 1. Joule heating of the vapor plasma, Q_j, which is given by J^2/σ, is also taken into account in these calculations.

4. Results

The energy density deposited on the divertor surface during a disruption can range from 10 to 200 MJ/m^2. Figure 2 shows a typical time evolution of tungsten surface temperature, melt-layer thickness, and vaporization losses

during a disruption for an incident plasma energy density of 10 MJ/m^2 deposited in a disruption time of 1 ms. An initial magnetic field strength of 5 T with an incident angle of 2° is assumed in this analysis. The sharp initial rise in surface temperature is due to the direct energy deposition of incident plasma particles at the material's surface. The following sharp decrease in surface temperature was caused by the shielding effect of the eroded material accumulated above the target surface. The subsequent surface temperature behavior is mainly determined by the energy flux from the emitted photon radiation in the vapor cloud and by the vapor-electron heat conduction. As more vapor is accumulated above the surface, the vapor becomes more opaque to photon radiation and therefore less energy is transmitted to the target surface. Because of the relatively low kinetic energy of the incident plasma particles ($E < 20$ keV), very little vapor is needed to completely stop incoming particles, particularly if the vapor is hot [13]. The total erosion depth due to surface vaporization is only a few micrometers, or about one to two orders of magnitude less than it would be if no vapor shielding was assumed [14].

The effect of disruption time on the hydrodynamic response of beryllium vapor is shown in Fig. 3 for disruption times of 0.1 and 1 ms. At the shorter disruption time, the deposited power is higher and causes both the solid/liquid and vapor temperatures to be much higher than those at the longer disruption time. The higher surface temperature causes more vapor to be emitted from the surface. The longer disruption time causes the vapor to expand to greater

distances above the divertor surface and also causes the energy flux deposited at the surface to diffuse deeper into the bulk and produce a thicker melt layer. The oblique magnetic field effectively limits vapor normal expansion to distances <30 cm above the target surface. This is important in reducing direct contact of the hot vapor with nearby components.

The temperature of the hot region of the vapor-cloud-generated plasma can range from a few eV up to few tens of eV, depending on the target material and on the incident plasma power density and particle kinetic energy. Significant radiation can be emitted from the hot vapor-front zones. In fact, in most high-power disruption cases, more than 80% of the incident plasma energy is converted to photon radiation. Figure 4 shows the emitted photon spectra from the hot beryllium vapor front during each disruption time. Because of the high power density at the shorter disruption time, the vapor cloud is strongly heated to much higher temperatures, causing the vapor to emit more intense radiation. A significant portion of the emitted radiation of low-Z materials is in line radiation. Depending on the intensity of vapor radiation, divertor design and configuration, and design of nearby components, the expanding hot vapor and its radiation may cause significant damage to these components. This is especially important in closed divertor configurations, which may be desirable for better plasma performance during normal operation [15]. Accordingly it is desirable that the vapor normal expansion be kept to a minimum and that the design of the divertor region not be of the closed type.

This is to allow the larger surrounding surface area to absorb the intense emitted radiation.

The vapor plasma however, just like the main reactor plasma, is also subject to MHD instabilities and possible loss of vapor confinement in front of incoming plasma particles. Initially, the cold vapor plasma with low conductivity, near the target surface, diffuses freely across magnetic field lines in the normal direction. This vapor plasma is heated by the main plasma particles and photon radiation as it expands above the surface and toward the main disrupting reactor plasma. The ionized vapor will then turn to follow the initial direction, $\mathbf{B}_o$, of the magnetic field lines, as shown schematically in Fig. 5. The magnetic field lines are assumed to be frozen into the surface of the liquid metal layer because of its high conductivity. Near the upper vapor boundary, the magnetic field lines become almost parallel to vapor surface. Figure 6 shows the magnetic field diffusion in beryllium vapor in relationship to distance normal to the target surface at two different disruption times. The expanding vapor plasma sweeps the magnetic field lines as it moves in the normal direction. Because of the more dense vapor plasma, i.e., higher pressure near the target surface during the shorter disruption time, magnetic field strength is sharply decreased to as little as 50% of its initial value. Because of such distortion in magnetic field lines and the resulting curvature, a flute-type of MHD instability can develop in the vapor-cloud plasma and causes the vapor to be removed away from the exposed surface, therefore reducing the vapor-shielding efficiency. In this work,

a preliminary model was developed to study the effects of vapor MHD instabilities during disruptions. When one side of the magnetic field is attached (target surface) and the other side is free (outer boundary), a balloon mode of flute instability can be developed [16]. The growth rate of the balloon mode instability can be estimated by

$$\gamma = \sqrt{\frac{B^2}{4\pi\rho}\frac{K_{\parallel}}{R_M}}, \tag{15}$$

where $K_{\parallel}$ is the instability wave number and R_M is radius of curvature of magnetic field lines (see Fig. 5). The wave number is given by $K_{\parallel} = 2\pi/\lambda_{\parallel}$, where $\lambda_{\parallel}$ is the wavelength of the instability.

For typical ITER disruption conditions, the frequency of this instability is calculated to be

$$\gamma > 10^5 \ s^{-1}. \tag{16}$$

Therefore, the necessary characteristic growth time for the instability to arise is

$$\tau_M = \gamma^{-1} < 10 \ \mu s. \tag{17}$$

This means that the vapor cloud can lose confinement in much less time than the total disruption time, $\tau_d > 100$ μs. However the vapor will take time to leave the unstable region above the surface. A turbulent mass diffusion coefficient for vapor loss is developed and implemented in the A*THERMAL-S code in which the vapor can be lost laterally along the surface, as well as normal to the surface. At each time step, a net vapor-mass loss from each vapor zone is calculated due to both classical diffusion across magnetic field lines and turbulent diffusion as a result of MHD instabilities.

Figure 7 shows the effect of MHD instabilities on beryllium vapor temperature and density as a function of density normal to surface for the indicated disruption conditions. The MHD instabilities limit vapor accumulation to only ≤ 2 cm above the target surface before the turbulent vapor diffuses away and disappear from the incoming disrupting plasma particles. However, there is enough vapor left to completely stop the incoming plasma particles and to continue shielding the target surface. The net erosion rate from surface vaporization in this case is increased by only a factor of ≈2 due to these MHD instabilities. For longer disruption times and higher energy deposition the erosion rate due to vapor loss can significantly increase. The turbulent diffusing hot vapor will then interact with nearby components and cause more erosion. The overall net erosion rate will depend on the disrupting plasma parameters, the size of disruption spot, design configuration, and the type of PFM. However,

for more accurate assessment of damage, a full 2-D analysis is needed with realistic component geometry. Such work is currently underway.

5. Simulation experiments

In current tokamak machines, ITER-like heat loads and disruption conditions are not achievable. Therefore, expected ITER conditions during a plasma disruption must be simulated in laboratory experiments. Laser light, electron beams, and plasma guns have been used in several countries to study disruption effects on candidate divertor materials. The majority of these experiments have near-reactor-relevant disruption parameters (i.e., heat loads of 10-20 MJ/m^2 and deposition time of <1 ms). Laser beam simulation usually produces higher erosion rates, mainly because vapor shielding is less important [17]. Because of the very small size of the laser beam (≈1 mm), the beam penetrates through the freely expanding vaporized material with little attenuation. Erosion from high-energy electron beams is also high due to the long range of electrons in both the resulting vapor cloud and the condensed phase material. Plasma gun devices, on the other hand, may more closely simulate tokamak plasma conditions during disruptions than both laser or electron beam devices.

The plasma-gun simulation experiment that is most relevant to ITER conditions is, however, the 2MK-200 facility located at TRINITI, Russia [18]. This

facility can produce deuterium plasma, in a magnetic field strength of up to 3 T, with total energy of up to 50 kJ and particle kinetic energy close to 1 keV. Power density can be as high as 10 MW/cm^2, but, with a maximum pulse duration of only ≤40 μs. Because of this limitation, 2MK-200 can be most useful only in studying the early stages of a tokamak disruption and the initial characteristics of plasma vapor interactions. Erosion measurement over the length of the pulse is very small compared to those expected during an ITER disruption.

Optical interferometry was used to determine the spatial distribution of plasma electron density and temperature in the evolving target vapor. The self-consistent model, with the multispecies mixture, implemented in A*THERMAL-S code was used to simulate a recent disruption experiment at the 2MK-200 facility. In the first 1 to 2 μs, a dense carbon vapor cloud ($N_e \approx 5 \times 10^{16}$ cm^{-3}) formed above the surface, and this is in good agreement with the experimental data [18]. Figure 8 shows experimental data and code simulation of the initial vapor cloud density and temperature. Due to the low kinetic energy of the ions in plasma gun simulation experiments (E_i << 10-20 keV), the density of the incident plasma particles is of the same order or higher than that of the vaporized target material. Therefore, it is necessary to take into account the influence of plasma particles on vapor hydrodynamics and on radiation transport. Initially, the deuteron plasma ions deposit their energy in target material and then in target vapor. Soon after, the density of the stopped plasma

particles becomes comparable and can exceed that of target vapor. After a few μs, almost pure deuteron plasma particles exist at the front region of the vapor cloud, as shown in Fig. 8. Most of the incoming energy is further deposited and stored as thermal energy in plasma particles. Part of this energy is transferred to the target vapor behind the mixture region, via electron heat conduction. The calculated electron temperature and density are in good agreement with measured data. In ITER, the situation is different. The density of the incoming plasma particles is much lower than that of the target vapor. Only a small fraction of the energy is stored as thermal energy. Most of the deposited energy is radiated from target vapor to divertor surface and nearby components, which can cause more erosion than expected from the gun experiments having the same initial disruption energy and deposition time.

The A*THERMAL-S code simulation results also agree well with electron beam experiments and the resulting vapor interferometry data [4]. Figure 9 compares the spatial distribution of vapor-cloud temperature above the exposed carbon target surface at two different electron beam facilities, i.e., the JEBIS facility at Naka, Japan [19], and the SOM facility at Efremov, Russia [20]. Because of the very high kinetic energy of these devices (100-150 keV), the electrons have a much longer range in both target material and vapor zone than in laser beam and plasma gun devices. Therefore, the deposited energy density in the vapor cloud is relatively low and the vapor is heated to lower

temperatures than in plasma gun experiments. No significant vapor radiation is therefore expected in the case of energetic electron beam deposition.

6. Conclusions

Detailed aspects of plasma disruption and simulation physics have been studied by using comprehensive self-consistent models that integrate in fine detail the structure's thermal evolution, physics of plasma/vapor interactions with multifluid mixing, magnetohydrodynamics, and photon radiation transport in a multilayer structure. Major differences are seen among current disruption simulation experiments and actual tokamak disruption, and therefore care should be used in interpreting and extrapolating these data to reactor conditions. Theoretical predictions of A*THERMAL-S and SPLASH codes are generally in good agreement with various experimental results. Vapor-produced plasma and its confinement are important in further reducing disruption damage to the divertor plate. Loss of vapor-plasma due to MHD instabilities, developed within the vapor, may significantly increase divertor erosion depending on the disrupting plasma parameters and divertor design. Photon radiation emitted from the vapor cloud as well as the turbulent diffusing vapor can also cause significant damage to nearby components. More-detailed modeling and more-reactor-relevant simulation experiments are required before a final judgment is made for the selection of PFMs. In general, plasma instabilities must be avoided or sharply minimized to only few disruptions during

reactor lifetime. Moreover, the effects of redeposited debris from the eroded and splashed materials on plasma contamination and on subsequent reactor operations must be studied and evaluated in detail.

Acknowledgments

This work is supported by the U.S. Department of Energy, Office of Fusion Energy, and by the Ministry of Atomic Energy and Industry, Russia.

References

[1] A. Hassanein et al., "Materials effects and design implications of disruptions and off-normal events in ITER," presented at 4th Int. Symp. on Fusion Technology, April 4-11, 1997, Tokyo, Japan, to be published in Fusion Eng. & Design.

[2] A. Hassanein, Fusion Technol. 30, No. 3, Part 2A (1996) 713.

[3] A. Hassanein, Fusion Technol. 19, No. 3, PART 2B (1991) 1789.

[4] A. Hassanein, Fusion Technol. 26 (1994) 532.

[5] A. Hassanein and I. Konkashbaev, Suppl. J. Nucl. Fusion 5 (1994) 193.

[6] A. Hassanein and I. Konkashbaev, J. Nucl. Mater. 220-222 (1995) 244.

[7] A. Hassanein and I. Konkashbaev, Fusion Eng. & Des. 28 (1995) 27.

[8] A. Hassanein and I. Konkashbaev, J. Nucl. Mater. 233-237 (1996) 713.

[9] A. Hassanein et al., to be published.

[10] A. Hassanein and I. Konkashbaev, "Erosion damage of nearby plasma-facing components during a disruption on the divertor plate," Proc. of 19th Symp. on Fusion Technology, Sept. 16-20, 1996, Lisbon, Portugal.

[11] A. Hassanein, Fusion Technol. 15 (1989) 513.

[12] A. Hassanein et al., "Modeling and simulation of melt-layer erosion during a plasma disruption," Proc. of 12th Int. Conf. on Plasma Surface Interactions in Controlled Fusion Devices, Saint-Raphael, France, May 20-24, 1996, to be published in J. Nucl. Mater.

[13] T. A. Mehlhorn, J. Appl. Phys., 52, (1981) 6522.

[14] A. Hassanein, "Response of Materials to High Heat Fluxes during Operation in Fusion Reactors," ASME, 88-WA/NE-2 (1988).

[15] G. Janeschitz et al., J. Nucl. Mater. 220-222 (1995) 73.

[16] G. Bateman, MHD Instabilities, MIT Press, Cambridge, MA, 1978.

[17] J. Van der laan, J. Nucl. Mater. 162-164 (1989) 964.

[18] N. Arkhipov et al., Proc. 18th Symp. on Fusion Tech., Karlsruhe, Germany, Aug. 22-26, 1994, Fusion Technol. Vol. 1 (1994) 395.

[19] P.D. Rockett, Sandia National Laboratories, personal communications.

[20] V. Engelko et al., J. Nucl. Mater. 220-222 (1995) 1071.

Figure Captions

Figure 1 Schematic illustration of different interaction zones during plasma instabilities.

Figure 2 Time evolution of tungsten surface temperature, melt layer, and eroded thickness following a plasma disruption.

Figure 3 Effect of disruption time on beryllium vapor temperature and density.

Figure 4 Photon radiation spectra emitted from beryllium vapor at two different disruption times.

Figure 5 Schematic illustration of magnetic field diffusion in vapor cloud.

Figure 6 Magnetic field diffusion in beryllium vapor above target surface for different disruption times.

Figure 7 Effect of MHD instabilities on beryllium vapor temperature and density normal to surface.

Figure 8 Comparison of plasma gun experiments and model calculations of carbon vapor temperature and concentration.

Figure 9 Comparison of electron beam experiments and model calculations of carbon vapor temperature.

Key Words:

(1) Plasma Disruptions.
(2) Vapor Shielding.
(3) MHD Instabilities.
(4) Erosion.
(5) Vaporization and Melting.
(6) Radiation Transport.

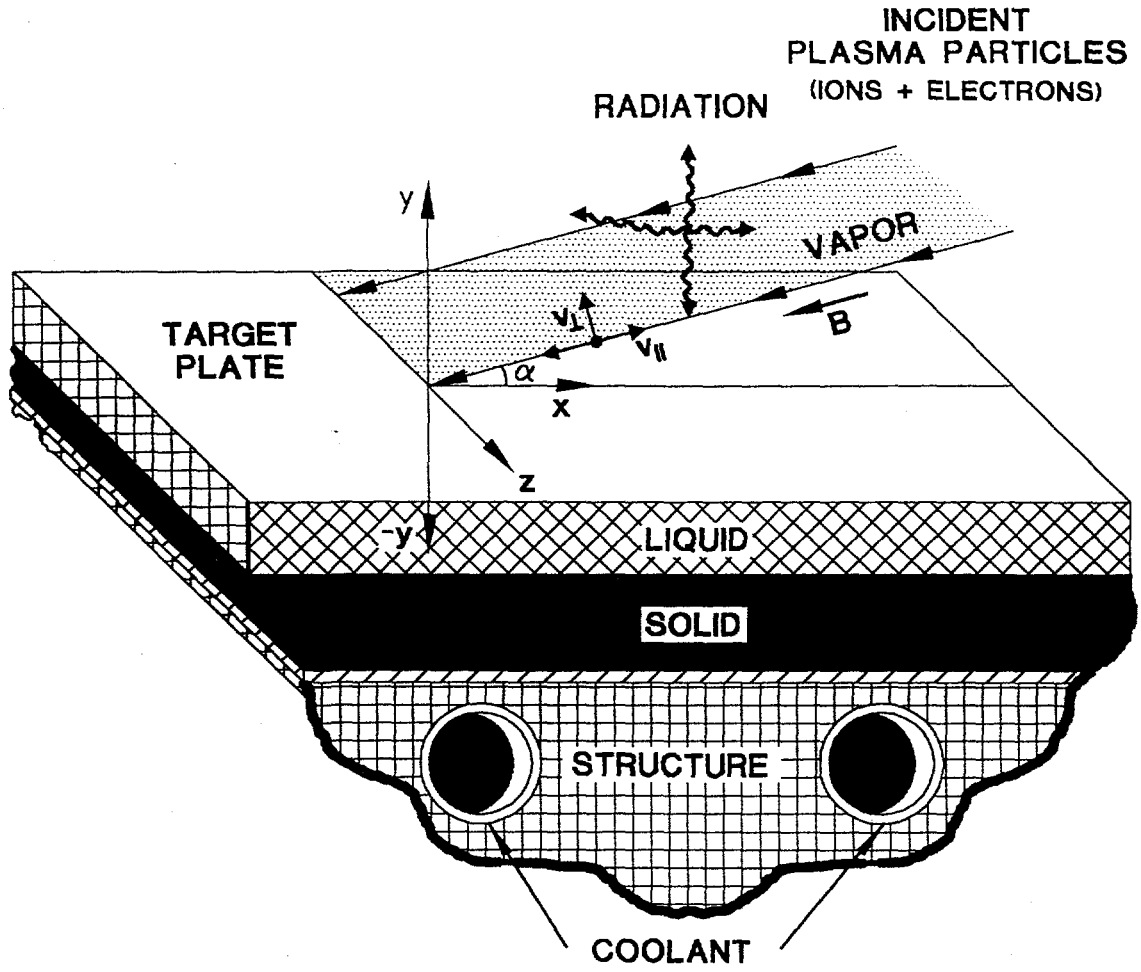

A. HASSANEIN

ARGONNE NATIONAL LABORATORY · UNIVERSITY OF CHICAGO

Fig (1)

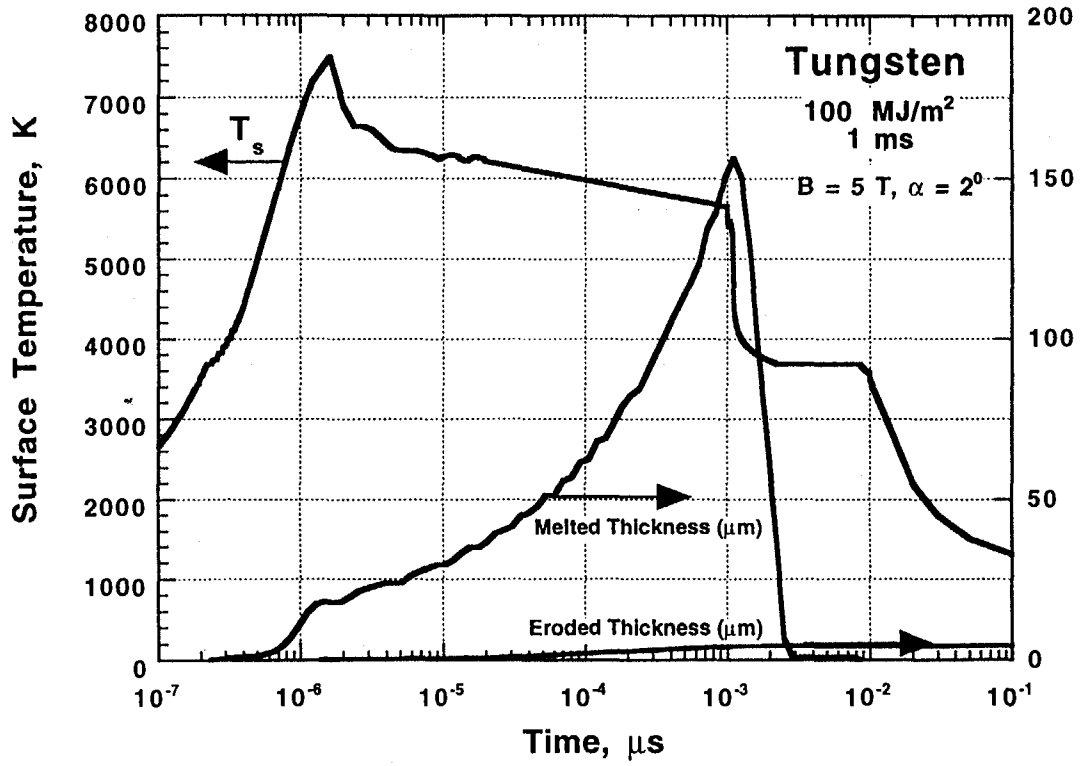
Tungsten
100 MJ/m²
1 ms
B = 5 T, α = 2⁰
T_s
Melted Thickness (μm)
Eroded Thickness (μm)
Surface Temperature, K
Time, μs
8000
7000
6000
5000
4000
3000
2000
1000
0
200
150
100
50
0
10⁻⁷
10⁻⁶
10⁻⁵
10⁻⁴
10⁻³
10⁻²
10⁻¹

Fig (2)

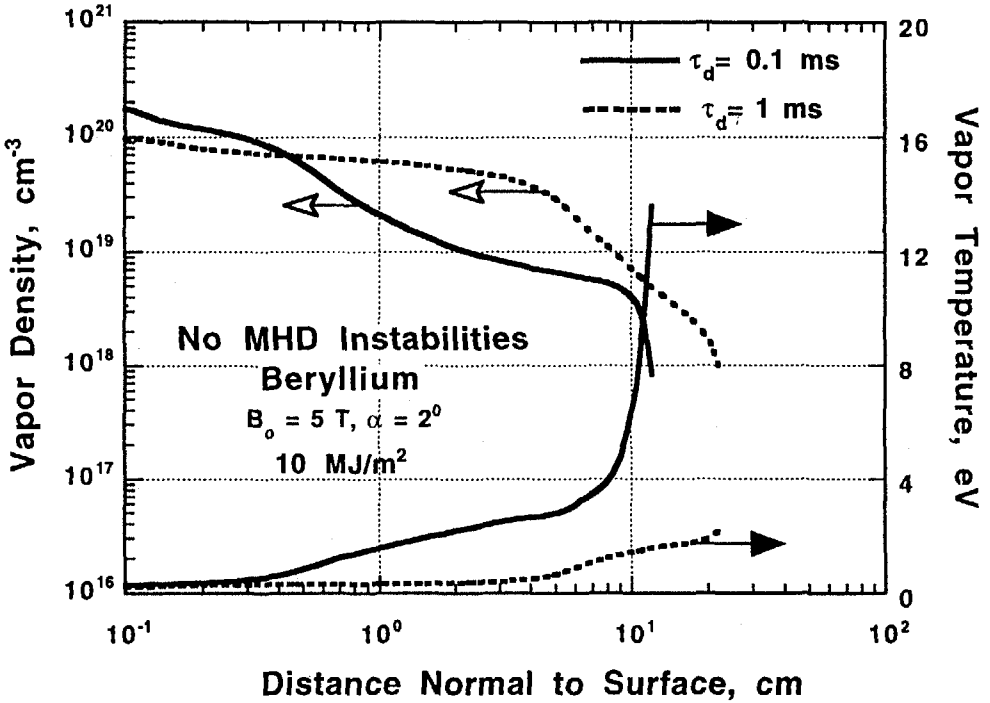
10^{21}
10^{20}
10^{19}
10^{18}
10^{17}
10^{16}
Vapor Density, cm^{-3}
20
16
12
8
4
0
Vapor Temperature, eV
τ_d= 0.1 ms
τ_d= 1 ms
No MHD Instabilities
Beryllium
B_o = 5 T, $\alpha = 2^0$
10 MJ/m^2
10^{-1}
10^0
10^1
10^2
Distance Normal to Surface, cm

Fig (3)

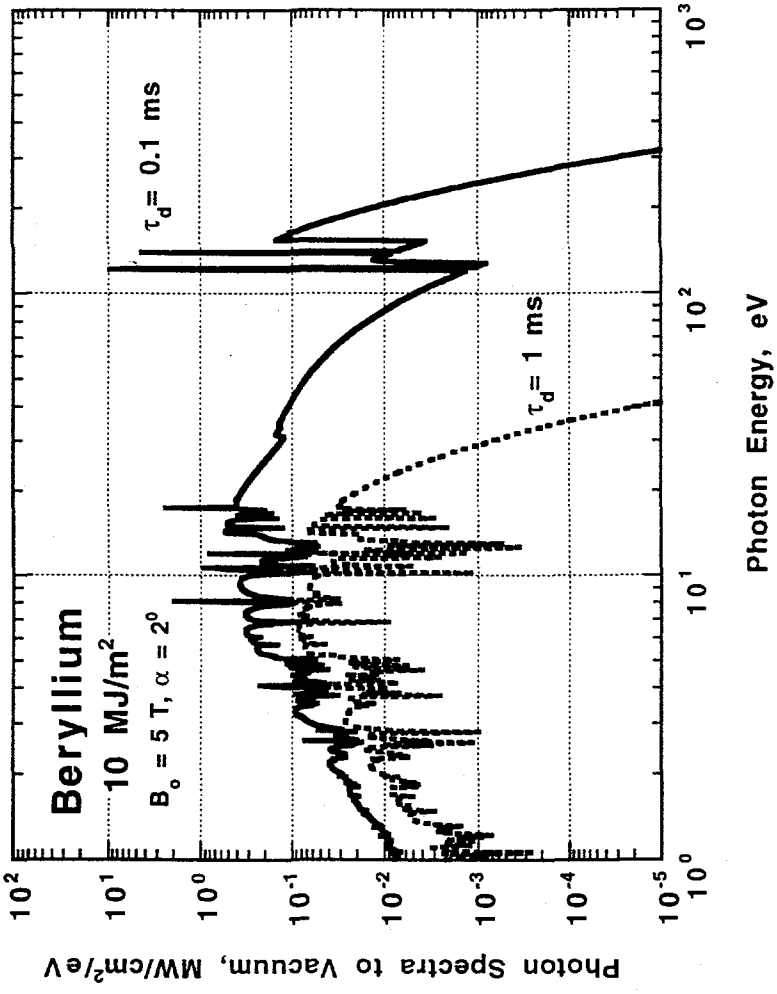
Beryllium
10 MJ/m²
B_o = 5 T, α = 2°
τ_d = 0.1 ms
τ_d = 1 ms
Photon Spectra to Vacuum, MW/cm²/eV
Photon Energy, eV
10²
10¹
10⁰
10⁻¹
10⁻²
10⁻³
10⁻⁴
10⁻⁵
10⁰
10¹
10²
10³

Fig 4

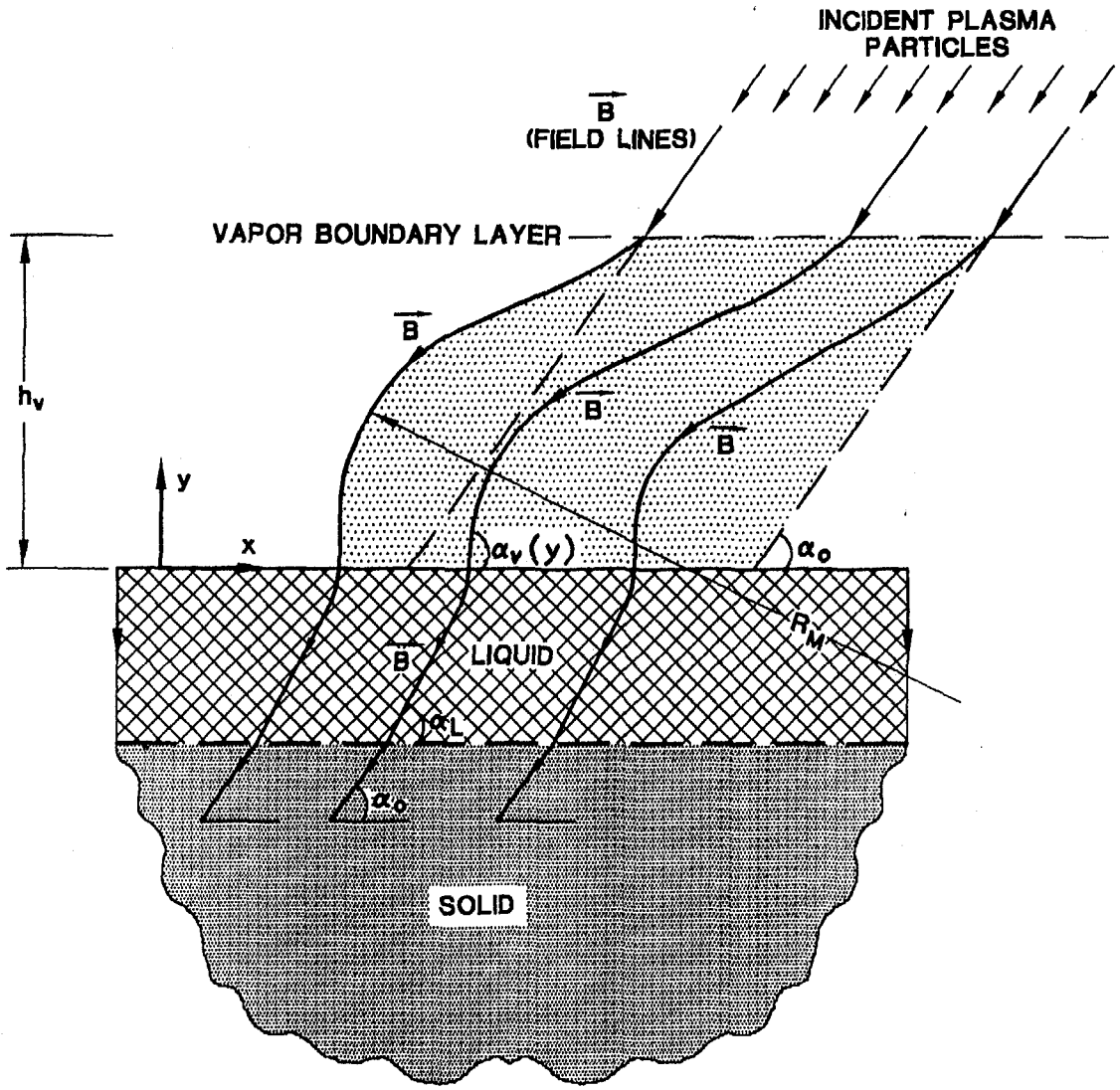

HASSANEIN

fig (5)

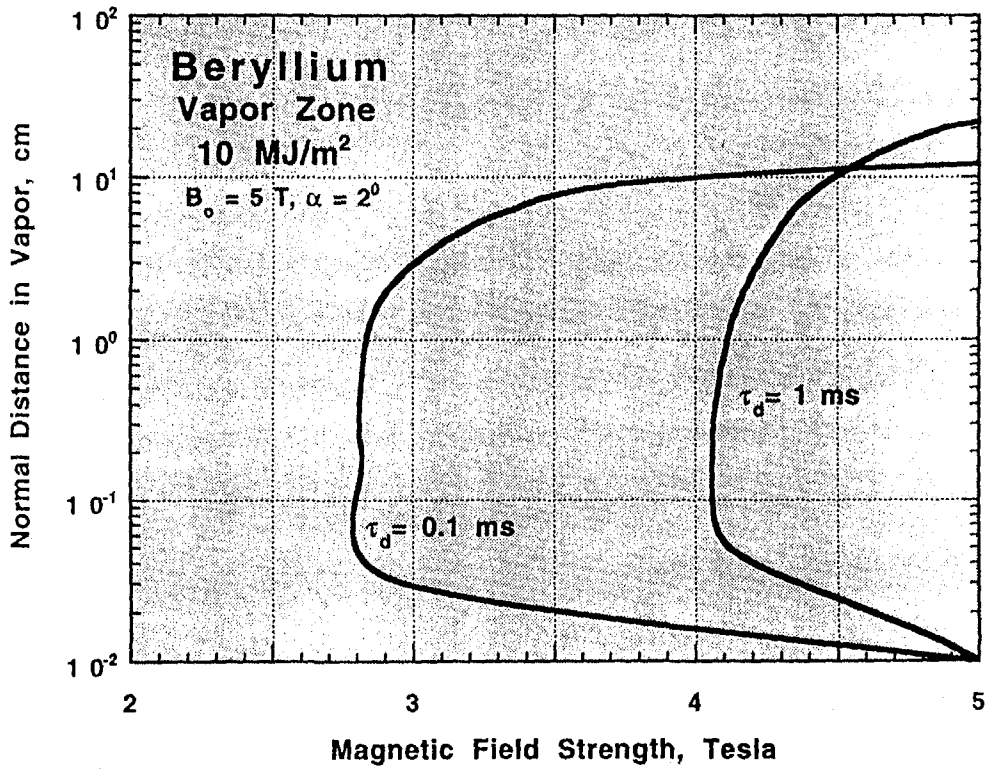
Beryllium
Vapor Zone
10 MJ/m²
B₀ = 5 T, α = 2⁰
τd= 1 ms
τd= 0.1 ms
Normal Distance in Vapor, cm
1 0²
1 0¹
1 0⁰
1 0⁻¹
1 0⁻²
2
3
4
5
Magnetic Field Strength, Tesla

Fig (6)

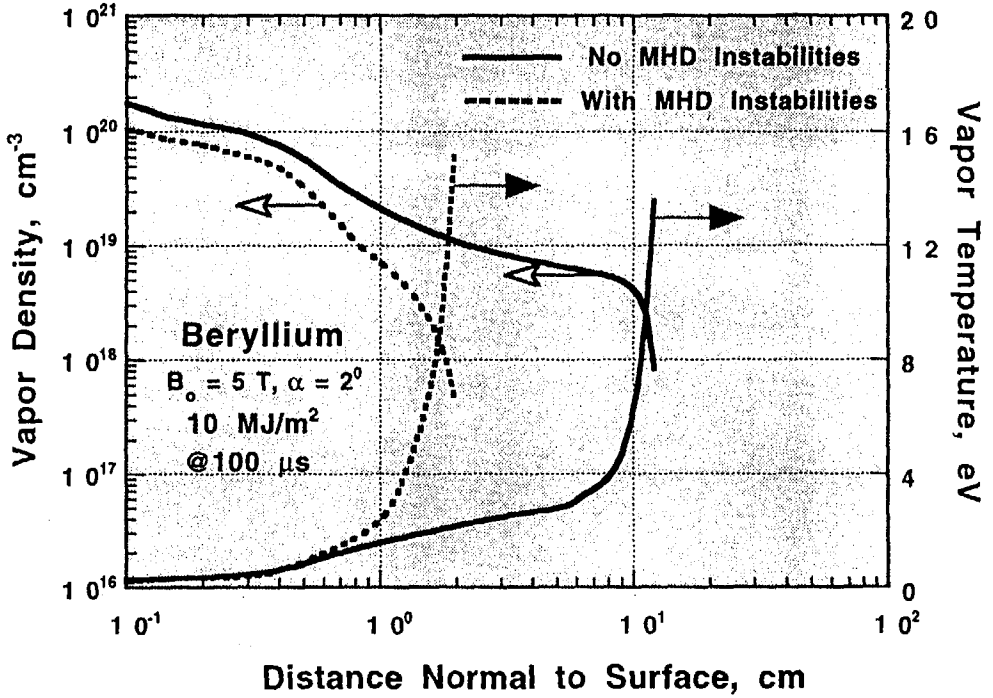
No MHD Instabilities
With MHD Instabilities
Beryllium
B_o = 5 T, $\alpha = 2^0$
10 MJ/m^2
@100 μs
Vapor Density, cm^{-3}
Vapor Temperature, eV
Distance Normal to Surface, cm
10^{21}
10^{20}
10^{19}
10^{18}
10^{17}
10^{16}
10^{-1}
10^{0}
10^{1}
10^{2}
20
16
12
8
4
0

Fig (7)

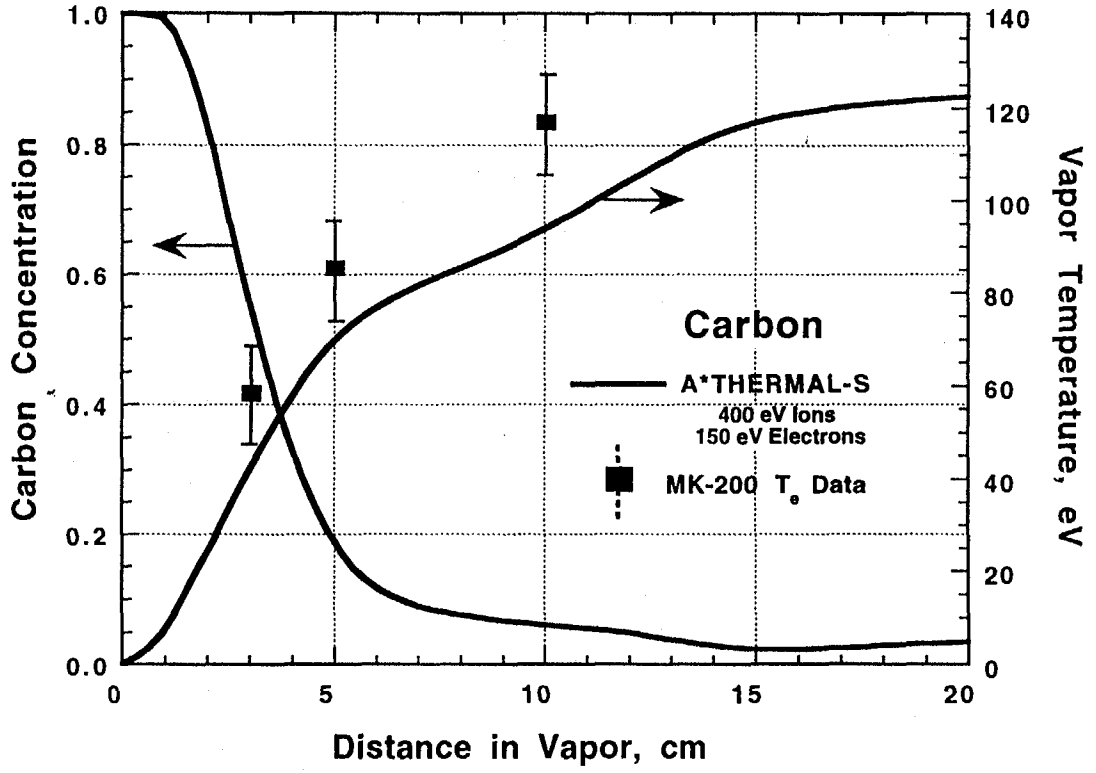
Carbon Concentration
Vapor Temperature, eV
Distance in Vapor, cm
1.0
0.8
0.6
0.4
0.2
0.0
140
120
100
80
60
40
20
0
0
5
10
15
20
Carbon
A*THERMAL-S
400 eV Ions
150 eV Electrons
MK-200 T_e Data

Fig (8)

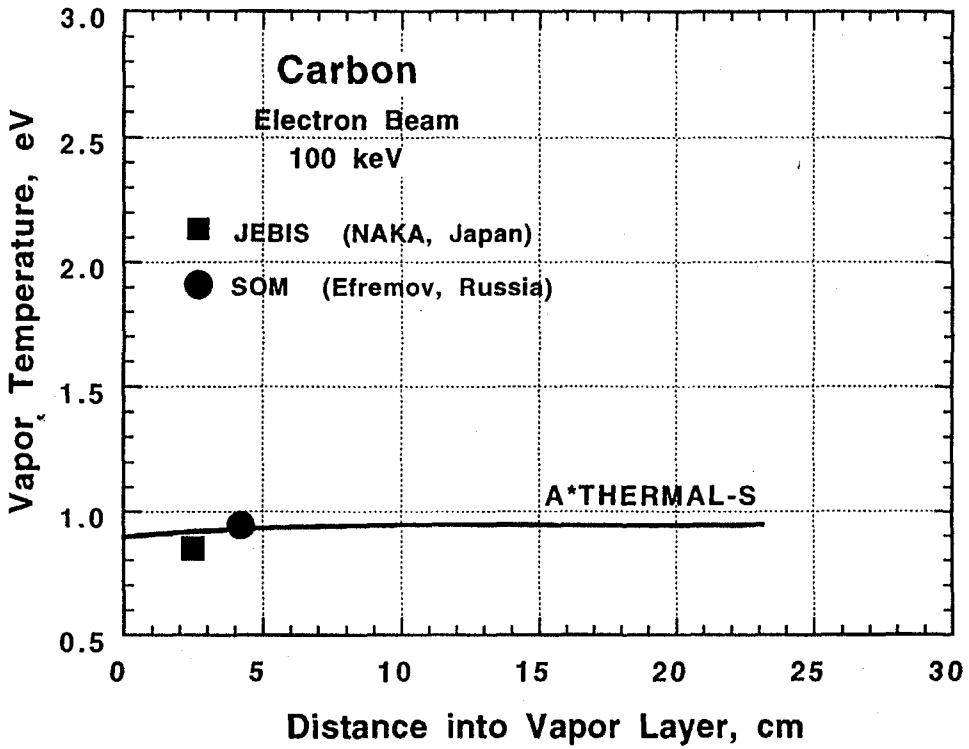
Carbon
Electron Beam
100 keV
JEBIS (NAKA, Japan)
SOM (Efremov, Russia)
A*THERMAL-S
Vapor Temperature, eV
Distance into Vapor Layer, cm
3.0
2.5
2.0
1.5
1.0
0.5
0
5
10
15
20
25
30

Fig (9)